A further investigation of effects of jet-disk separation distance on steady mixed convective vortex flow resulting from a confined impinging air jet

K.M. Chen, F.C. Hsieh, J.C. Hsieh, T.F. Lin *

Department of Mechanical Engineering, National Chiao Tung University, Hsinchu 30010, Taiwan, ROC

ABSTRACT

We extend our previous study [J.C. Hsieh, T.F. Lin, Effects of jet-to-disk separation distance on the characteristics of mixed convective vortex flow in an impinging air jet confined in a cylindrical chamber, Int. J. Heat Mass Transfer 48 (2005) 511–525] here to further investigate how the jet-disk separation distance H affects the mixed convective vortex flow resulting from a round air jet impinging onto a heated horizontal circular disk confined in a vertical cylindrical chamber. The experiment is conducted for the jet-disk separation distance varying from 40.0 to 60.0 mm and the jet flow rate is varied from 0 to 12.0 slpm (standard liter per minute) for the jet Reynolds number Re_j ranging from 0 to 1623. The temperature difference between the disk and the air injected into the chamber is varied from 0 to 25.0 °C for the Rayleigh number Ra ranging from 0 to 507,348. The data from the present study for the ratio H/D_j = 4–6 are compared with our previous study for H/D_j = 1–3. The results indicate that the critical jet Reynolds numbers for the onsets of the secondary and tertiary inertia-driven rolls and for the onset of the buoyancy-driven roll vary nonmonotonically with the jet-disk separation distance due to the complicate changes of the vortex flow structure with H. In the steady vortex flow, both the primary inertia-driven roll and the buoyancy-driven roll get larger at increasing jet-disk separation distance before they contact with each other for H/D_j = 1 and 2. But for $H/D_j \geq 3$ the primary roll and buoyancy roll do not always grow at increasing H. Finally, empirical correlations are proposed for the critical conditions leading to the onsets of the inertia- and buoyancy-driven vortex rolls.

© 2009 Elsevier Ltd. All rights reserved.

1. Introduction

Considerable amount of work has been carried out in the past to investigate the fluid flow and heat transfer in the round or slot jet impinging onto a large horizontal plate. Most of the studies focus on quantifying the highly efficient heat transfer associated with the high speed impinging jets. Thus the flow driven by the jet inertia is much stronger than the flow driven by the buoyancy. For instance, to explore the detailed vortex flow structure, Fitzgerald and Garimella [2] and Morris et al. [3,4] used numerical simulation and flow visualization to investigate the vortex flow characteristics for a liquid impinging jet, which were found to be influenced by the jet Reynolds number and jet-disk separation distance. For the applications such as growth of semiconductor thin crystal films on heated silicon wafers through the chemical vapor deposition (CVD) processes, low speed impinging jets are often employed and the buoyancy-driven secondary flow can be relatively strong. Recently, the vortex flow structures resulting from a low speed gas jet impinging onto a heated horizontal disk confined in a vertical cylindrical chamber at low Re_j were visualized by Hsieh et al. [5], which showed that the inertia and buoyancy-driven gas flow recir-

culation was typically in the form of three circular vortex rolls. In addition, the effects of the jet Reynolds number and jet-disk separation distance on the locations of the centers of the primary and secondary inertia-driven vortex rolls were investigated by Law and Masliyah [6]. Details on the size and locations of these vortex rolls affected by the jet Reynolds and Richardson numbers for a laminar confined slot jet were examined by Sahoo and Sharif [7]. For a confined laminar slot impinging jet the critical jet Reynolds number for the onset of unsteady flow was numerically shown to be between 585 and 610 by Chiriac and Ortega [8]. According to the turbulence intensity measurement at a nozzle exit, Lin et al. [9] suggested that the jet at a Reynolds number smaller than 1226 may be regarded as in an initially laminar flow regime. Santen et al. [10,11] indicated that the onset of thermal instability became earlier at increasing buoyancy-to-inertia ratio. Moreover, a laminar impinging jet with small pulsation at the outlet of the jet was numerically simulated by Poh et al. [12]. Law and Masliyah [13] found that the impinging jet flow structure was significantly influenced by the chamber geometry. More complete information on the flow associated with the impinging jets can be found from the critical reviews by Jambunathan et al. [14], and Viskanta [15].

As mentioned above, the gas jet impinging onto the substrate in the CVD chamber is at relatively low flow rate and the buoyancy in the flow is no longer small compared with the jet inertia with the

---

* Corresponding author. Tel.: +886 35 712121x55118; fax: +886 35 726440.
E-mail address: tflin@mail.nctu.edu.tw (T.F. Lin).

Nomenclature

D_j	diameter of jet at the injection pipe exit (mm)
Gr	Grashof number, $g\beta\Delta T H^3/v^2$
g	gravitational acceleration (m/s^2)
H	jet-to-disk separation distance (mm)
HD_j	ratio of the jet-disk separation distance to the jet diameter, H/D_j
Q_j	jet flow rate (standard liter per minute, slpm)
r, θ, z	dimensional coordinates in cylindrical coordinate system
R, Θ, Z	dimensionless coordinates r/R_c, $\theta/360°$ z/H
Ra	Rayleigh number, $g\beta\Delta T H^3/\alpha v$
Re_j	jet Reynolds number, $\overline{V}_j D_j/v$
Re_w	local Reynolds number of the flow in the wall-jet region, $\bar{u}H/v$
Re_{we}	local Reynolds number of the flow in the wall-jet region at disk edge, $\bar{u}_{we}H/v$
R_w	radius of disk (mm)
T_a	ambient temperature (°C)
T_f	temperature of the heated disk (°C)

T_j	temperature of jet at the injection pipe exit (°C)
$\bar{u}$	average radial velocity of the flow in the wall-jet region, $Q_j/(2\pi r H)$
$\bar{u}_{we}$	average radial velocity of the flow in the wall-jet region at disk edge, $Q_j/(2\pi R_w H)$
$\overline{V}_j$	average velocity of the air jet at the injection pipe exit (m/s)

Greek symbols

α	thermal diffusivity (m^2/s)
β	thermal expansion coefficient (1/K)
ΔT	temperature difference between the heated disk and the air injected into the chamber (°C)
v	kinematic viscosity (m^2/s)
Φ	non-dimensional temperature, $(T - T_j)/(T_f - T_j)$
ρ	density (kg/m^3)
μ	dynamic viscosity (kg/ms)
k	thermal conductivity (W/m °C)

Reynolds and Rayleigh numbers, respectively, ranging from 0.01 to 100.0 and from 10,000 to 1,000,000. The importance of the buoyancy on the recirculating flow in a vertical CVD reactor was demonstrated by Wahl [16]. Similar investigations have been carried out for various types of the metal organic CVD reactor [17–19]. Recently, Vanka and his colleagues [20,21] conducted a series of computational studies to explore the effects of the flow rate, substrate rotation rate, and chamber geometry on the flow in impinging jet CVD reactors. Burwash et al. [22] reported that increasing the ratio of the jet-disk separation distance to the jet diameter could result in higher deposition efficiency and deposition density around the stagnation point on a wafer.

The above literature review clearly indicates that the chamber geometry plays an important role in the vortex flow induced in the chamber. More specifically, at increasing jet-disk separation distance the interactions between the inertia and buoyancy-driven vortex flows are expected to be more intense. Obviously, shortening the jet-disk separation distance is beneficial in suppressing the buoyancy-driven flow recirculations since Ra is proportion to H^3. But a small jet-disk separation distance is more likely to cause unwanted vapor deposition on the jet nozzle and top wall of the processing chamber. In the present study, we extend our earlier study [1] to further investigate the effects of the jet-disk separation distance on the characteristics of the vortex flow in a laminar jet impinging onto a horizontal heated disk confined in a vertical cylindrical chamber with a larger jet-disk separation distance (HD_j = 4–6). The results will be compared with those in our previous study [1] for HD_j = 1–3.

2. Experimental apparatus and procedures

In order to conduct the experiment at reasonably low cost, we use air as the working fluid in the present experiment to replace the inert gases normally employed in real CVD processes. In view of the similar thermodynamic and thermophysical properties for various gases, the results obtained here are still applicable to the CVD system. The experimental system established in our previous study [5] is employed here to investigate the effects of the jet-disk separation distance on the characteristics of inertia and buoyancy-driven vortex flow resulting from a round air jet impinging onto a

heated horizontal circular disk confined in a vertical cylindrical chamber. A schematic of the experimental system is shown in Fig. 1. The present experimental system consists of five major parts: gas injection unit, processing chamber, heating unit, flow visualization unit, and temperature measurement unit.

The gas injection unit consists of a 2 HP air compressor, a flow meter, a smoke generator, filters, pressure regulator, and connection and injection pipes. In the experiments, the air is drawn from the ambient by the compressor and sent into a 300-L and 100-psi high-pressure air tank and is filtered to remove moisture and tiny particles. Then, the air is mixed with smoke tracers in the smoke generator. It is later injected into the processing chamber through the injection pipe which is coaxial with the processing chamber. The injection pipe diameter is fixed at 10.0 mm and the pipe is thermally well insulated by a superlon insulation layer of 16.0-mm thick. The straight portion of the pipe is 600.0-mm long. This length of the constant cross-section portion of the injection pipe is selected to ensure that it is long enough to have a fully developed air flow at the outlet of the injection pipe. The air temperature at the cross section 600.0 mm upstream of the injection pipe exit is measured by a T-type thermocouple. The measured value is considered as the temperature of the air injected into the processing chamber in view of the good thermal insulation over the pipe.

The processing chamber, which is made of 6.0-mm thick quartz glass to allow for the observation of the flow pattern in the chamber, is cylindrical and has a diameter of 291.0 mm. The distance between the chamber top and bottom is 200.0 mm. To facilitate the flow visualization, the chamber top is made of an acrylic plate. Air is injected vertically downward from the injection pipe into the cylindrical chamber and impinges directly onto the heated disk. The outside surface of the chamber is thermally well insulated by a superlon insulator of 10.0-mm thick. The insulator can be opened during the flow visualization experiment.

The heating unit is designed to maintain the circular disk at the preset uniform temperature during the experiment. It is composed of a 10.0-mm thick copper plate of eight-inch in diameter, acting as the disk, placed above another 20.0-mm thick copper plate of the same diameter, which is heated by D.C. power supplies. The lower copper plate is then placed on a bakelite plate. A gap height of 1 mm is kept between the two copper plates allowing the thermal radiation and convection to transfer heat from the lower to upper
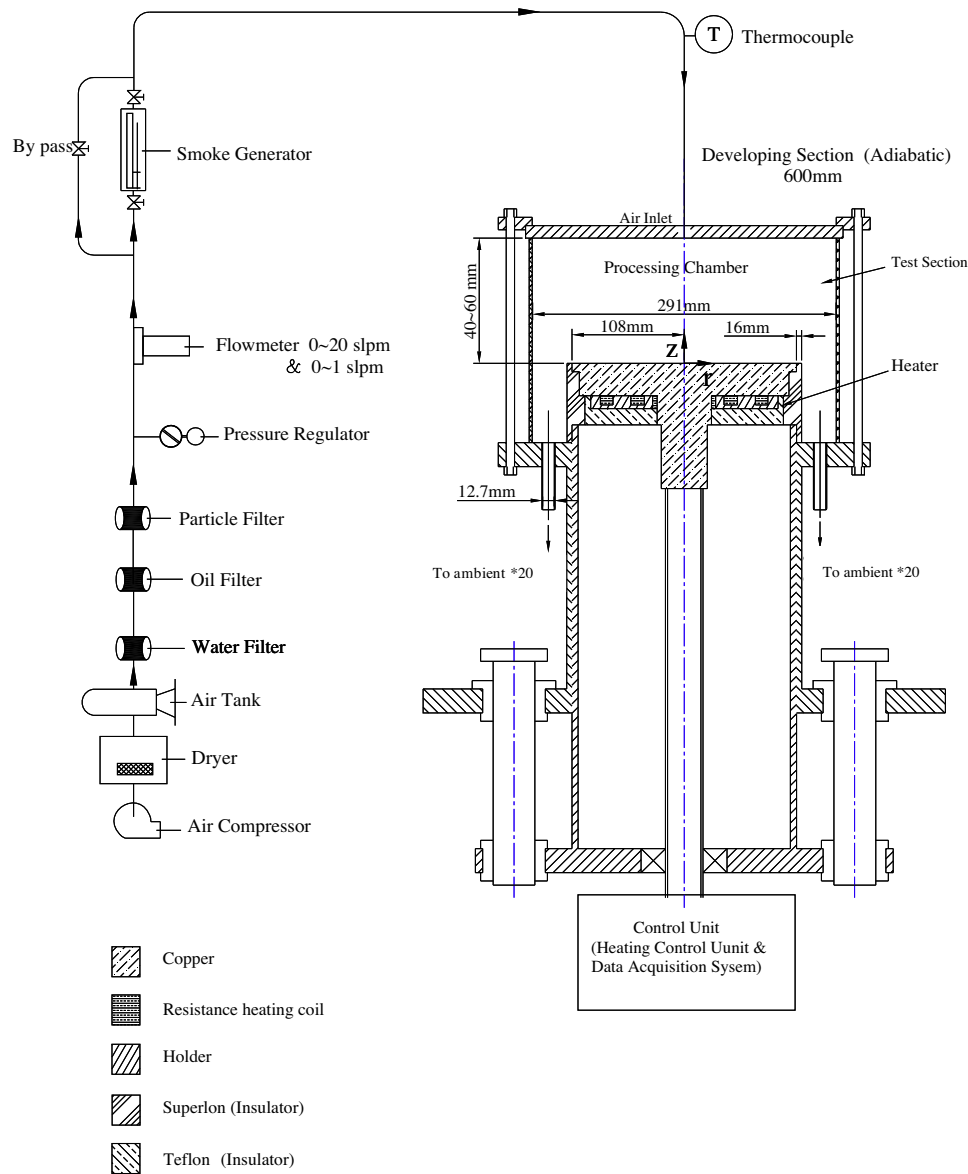
Fig. 1. Schematic diagram of the experimental system.

plates. The heater attached onto the back side of the lower copper plate is divided into three concentric zones. Each zone is independently heated by a power supply. Additionally, to reduce the significant energy loss from the sidewall of the copper plates and Teflon plate, the lateral surface of the entire heating unit is wrapped with a 16.0-mm thick thermal insulation layer of superlon. A proper control of the currents transferred from the power supplies to the heating coils leads to a nearly uniform disk temperature with a maximum deviation of 0.1 °C across the disk. The temperature of the upper copper plate at selected detection points is measured by three T-type thermocouples inserted into the plate by the small holes drilled on the backside of the plate.

A smoke-tracer flow visualization technique is employed to observe the flow patterns induced by the air jet impinging onto the heated disk in the cylindrical chamber. The smoke is produced from burning incense prepared from sandalwood. The smoke is mixed uniformly in the smoke generator and is carried out by the inlet air and then sent into the cylindrical chamber. The gas flow pattern in the chamber is illuminated by the vertical and horizontal plane light sheets produced by passing parallel lights from

an overhead projector through adjustable knife edges. The time variations of the flow pattern from the side view are recorded by the Sony digital video camera DCR-PC330.

The air temperature in the processing chamber is measured by inserting a calibrated and corrected thermocouple probe into the chamber through 24 holes of 1.0 mm in diameter opened at the selected locations on the top of the chamber. The thermocouple probe is an OMEGA (model HYPO) hypodermic extremely small T-type thermocouple implanted in a 2.0-in. long stainless steel hypodermic needle.

Uncertainties in the Rayleigh number, jet Reynolds number and other independent parameters are calculated according to the standard procedures established by Kline and McClintock [23]. The uncertainties of the thermophysical properties of air are also included in the analysis. In addition, the uncertainties of the control unsteadiness and temperature non-uniformity are accounted for in the evaluation of the data uncertainty. The analysis shows that the uncertainties of temperature, volume flow rate, Re_j, Ra, and HD_j measurements are estimated to be less than ±0.2 °C, ±2%, ±2.3%, ±8.6%, and ±0.5%, respectively.

3. Results and discussion

In the present experiment the air flow in the chamber is at the atmospheric pressure. Three jet-disk separation distances are considered with H = 40.0, 50.0 and 60.0 mm for the jet flow rate Q_j ranging from 0 to 12.0 slpm and the temperature difference between the disk and the air injected into the chamber ΔT is varied from 0 to 25.0 °C. Some data from the previous study will be included here for comparison purpose. The dimensionless groups governing the flow are the ratio of the jet-disk separation distance to the injection pipe diameter, jet Reynolds number, and Rayleigh number (Grashof number). They are, respectively, defined as

$$HD_j = \frac{H}{D_j} \tag{1}$$

$$Re_j = \frac{V_j D_j}{\nu} = \frac{4}{\pi} \frac{Q_j}{\nu D_j} \tag{2}$$

$$Ra = \frac{g\beta\Delta T H^3}{\alpha\nu} \tag{3}$$

$$Gr = \frac{g\beta\Delta T H^3}{\nu^2} = Ra/Pr \tag{4}$$

Thus in the present study HD_j, Re_j, and Ra, respectively, vary from 4 to 6, 0 to 1623, and 0 to 507,348. Moreover, it is noted that the local buoyancy-to-inertia ratio for the wall-jet flow at the disk edge is an important parameter in dealing with the onset of the buoyancy-driven roll [1]. It can be expressed as

$$\frac{Gr}{Re_{we}^2} = \left(\frac{Gr}{Re_j^2}\right) \cdot \left(\frac{8R_w}{D_j}\right)^2 \tag{5}$$

In what follows selected flow photos taken from the flow visualization and the measured temperature data are examined closely to delineate how the gas flow characteristics are affected by the jet-disk separation distance.

3.1. Effects of HD_j on onset of inertia-driven vortex rolls

The effects of the jet-disk separation distance on the critical conditions for the appearance of the inertia-driven vortex rolls are illustrated first. Here we investigate the onset of the inertia-driven rolls by visualizing the vortex flow in the chamber at various Re_j for an unheated disk (Ra = 0) at increasing Re_j until the vortex rolls start to appear. Note that the lowest jet flow rate which can be accurately resolved in the present experimental apparatus is 0.1 slpm. Even at this small Q_j the primary inertia-driven roll is already seen in the chamber for all jet-disk separation distances tested here (H = 10.0–60.0 mm). Furthermore, for a continuing increase in Re_j, the secondary and tertiary inertia-driven rolls appear in sequence resulting from the shearing effect of the strong primary roll, which is already discussed in the previous study [1].

Table 1 summarizes the present data for the onset condition of the steady secondary and tertiary inertia-driven rolls at various jet-

Table 1
Critical condition for appearance of the inertia-driven vortex flow (ΔT = 0 °C).

Vortex roll	Separation distance (H, mm)	Flowrate (Q_j, slpm)	Re_j
Secondary inertia-driven roll	10.0	1.8	243
	20.0	1.3	176
	30.0	0.8	108
	40.0	1.5	203
	50.0	X	X
	60.0	X	X
Tertiary inertia-driven roll	10.0	5.5	744
	20.0	5.0	676
	30.0	4.6	622
	40.0	4.6	622
	50.0	5.7	771
	60.0	5.2	703

The roll does not appear in the range of the parameter tested in the present study, X.
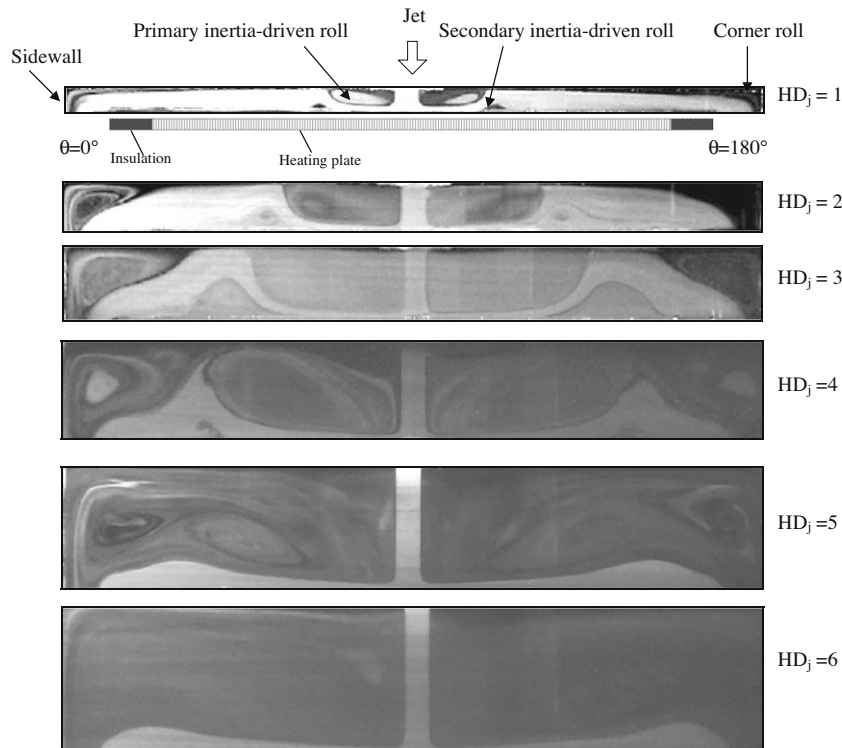

Fig. 2. Steady side view flow photos taken at the cross plane θ = 0° and 180° for various HD_j at ΔT = 0 °C (Ra = 0) and Q_j = 2.0 slpm (Re_j = 270).

disk separation distances. It is of interest to note from these results that at a small jet-disk separation distance for HD_j increased from 1 to 3 the onset of the secondary inertia-driven roll becomes earlier but the onset is delayed to a higher Re_j at a larger jet-disk separation distance for HD_j raised from 3 to 4. This nonmonotonic variation in the critical Re_j for the onset of the secondary roll at increasing HD_j can be attributed to the unusual change of the secondary roll with HD_j shown in Fig. 2. The results indicate that for $HD_j \leqslant 3$ the primary, secondary and corner rolls all grow in size for an increase in HD_j. But for HD_j raised from 3 to 4 both the primary inertia-driven roll and corner roll also grow substantially in size while the secondary roll is squeezed to become smaller. So the critical jet Reynolds number for the onset of the secondary roll for $HD_j = 4$ is higher. Note that the secondary roll is not seen in the chamber for $HD_j = 5$ and 6, which could be ascribed to the growth of the primary roll at increasing HD_j and it directly contacts with the corner roll at this high HD_j. No space is available for the secondary roll. In fact, for $HD_j = 5$ and 6 the secondary roll is not induced in the entire range of the Q_j tested in the present study.

The typical pattern of the tertiary inertia-driven vortex roll for HD_j varied from 1 to 6 is shown in Fig. 3. The flow is axisymmetric even for the cases without steady state at long time for a high Re_j ($HD_j = 4$–6), and hence only the side view flow photos at the vertical plane $\theta = 0°$ are given here. The data in Table 1 indicate that the onset of the tertiary roll takes place at lower Re_j as HD_j increases from 1 to 3. This is simply because the primary inertia-driven roll is stronger at higher HD_j for a given Re_j, which in turn causes an earlier onset of the tertiary roll. However, the onset of the tertiary roll is delayed to a higher Re_j for HD_j raised from 4 to 5. This is conjectured to result from the fact that for $HD_j = 5$ no secondary roll appears and the primary roll nearly occupies the entire chamber at a high Re_j. Thus it is more difficult for the tertiary roll to be induced. But the critical Re_j for the onset of the tertiary roll becomes smaller for a stronger primary roll as HD_j is raised further from 5 to 6. It is noted from Fig. 3 that the vortex flow structures in the chamber for $HD_j = 5$ and 6 are significantly different from that for $HD_j = 1$–4 as the tertiary roll starts to appear in the chamber, which in turn results in the nonmonotonic variation in the critical Re_j for the onset of the tertiary roll at increasing HD_j.

Finally based on the present data given in Table 1, the onset conditions of the secondary and tertiary rolls can be expressed as

(a) for the secondary inertia-driven roll

$$Re_j = 296.8 - 61.3 \times HD_j^2 + 13.8 \times HD_j^3 \qquad (6)$$

for $1 \leqslant HD_j \leqslant 4$ and $108 \leqslant Re_j \leqslant 243$

(b) for the tertiary inertia-driven roll

$$Re_j = 1489.3 - 719.5 \times HD_j + 191 \times HD_j^2 - 15.5 \times HD_j^3 \quad (7)$$

for $2 \leqslant HD_j \leqslant 6$ and $622 \leqslant Re_j \leqslant 771$.

When compared with our experimental data, the standard deviations of Eqs. (6) and (7) are, respectively, 7.2% and 5.5%.

3.2. Effects of HD_j on onset of buoyancy-driven vortex roll

Next, the onset of the buoyancy-driven vortex roll is examined. When there is a temperature difference between the jet and disk the buoyancy-driven roll begins to appear in the region near the heated disk edge as Re_j is decreased to a certain value for a given Ra. Fig. 4 shows some vortex flow patterns for the cases with the absence and presence of the buoyancy roll for various Re_j and HD_j at $\Delta T = 5$ °C. The measured critical values for the onset of buoy-
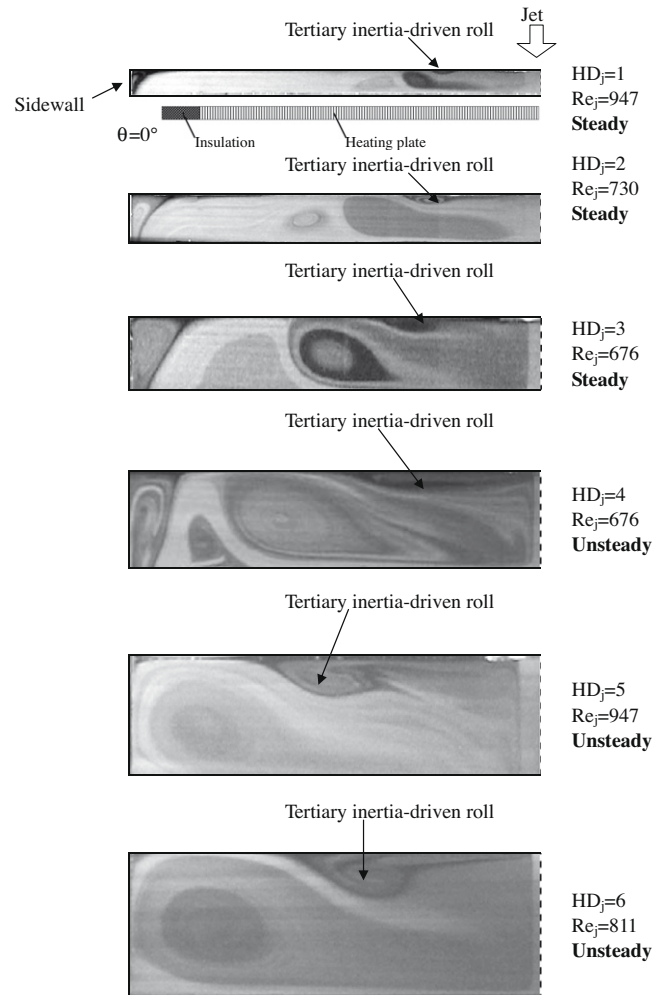

Fig. 3. Side view flow photos taken at the cross plane for various HD_j and Re_j with the disk unheated ($\Delta T = 0$ °C).

ancy roll for various H are summarized in Table 2. The buoyancy roll appears as the jet Reynolds number is below the critical value listed in the table. The data show that the critical Q_j for the onset of buoyancy-driven roll is higher for a higher ΔT, indicating that the buoyancy force is higher at a higher ΔT and the buoyancy roll can appear in a wider range of Re_j. It is also noted from the table that for $H = 20.0$–40.0 mm the buoyancy-driven vortex roll always appears at certain higher ΔT even for Q_j is raised to the highest level of 12.0 slpm tested here. Moreover, it is of interest to note from the experiment that the buoyancy roll always appears at the intermediate H of 30.0 mm for $\Delta T \geqq 0.5$ °C. The data given in Table 2 indicate the onset of the buoyancy roll for the small jet-disk separation distance with $H = 10.0$ and 20.0 mm occurs at a constant local buoyancy-to-inertia ratio at the disk edge Gr/Re_{we}^2, as already observed in the previous study [1,5]. However, this is not the case for $H \geqq 40.0$ mm. In fact, the critical buoyancy-to-inertia ratio increases significantly with H for a larger jet-disk separation distance with $H = 40.0$–60.0 mm. This can be attributed to the fact that only the primary inertia-driven roll and buoyancy-driven roll exist in the chamber and they are in close contact for $H = 40.0$–60.0 mm (Fig. 4), unlike that for $H = 10.0$ and 20.0 mm in which the inertia and buoyancy-driven rolls separate from each other. So the critical Gr/Re_{we}^2 for the onset of buoyancy roll needs to be higher to overcome the stronger mutual pushing of the two rolls at a higher H. Moreover, at the same ΔT the critical Q_j for the onset of buoyancy roll increases for HD_j raised from 1 to 2 but decreases for
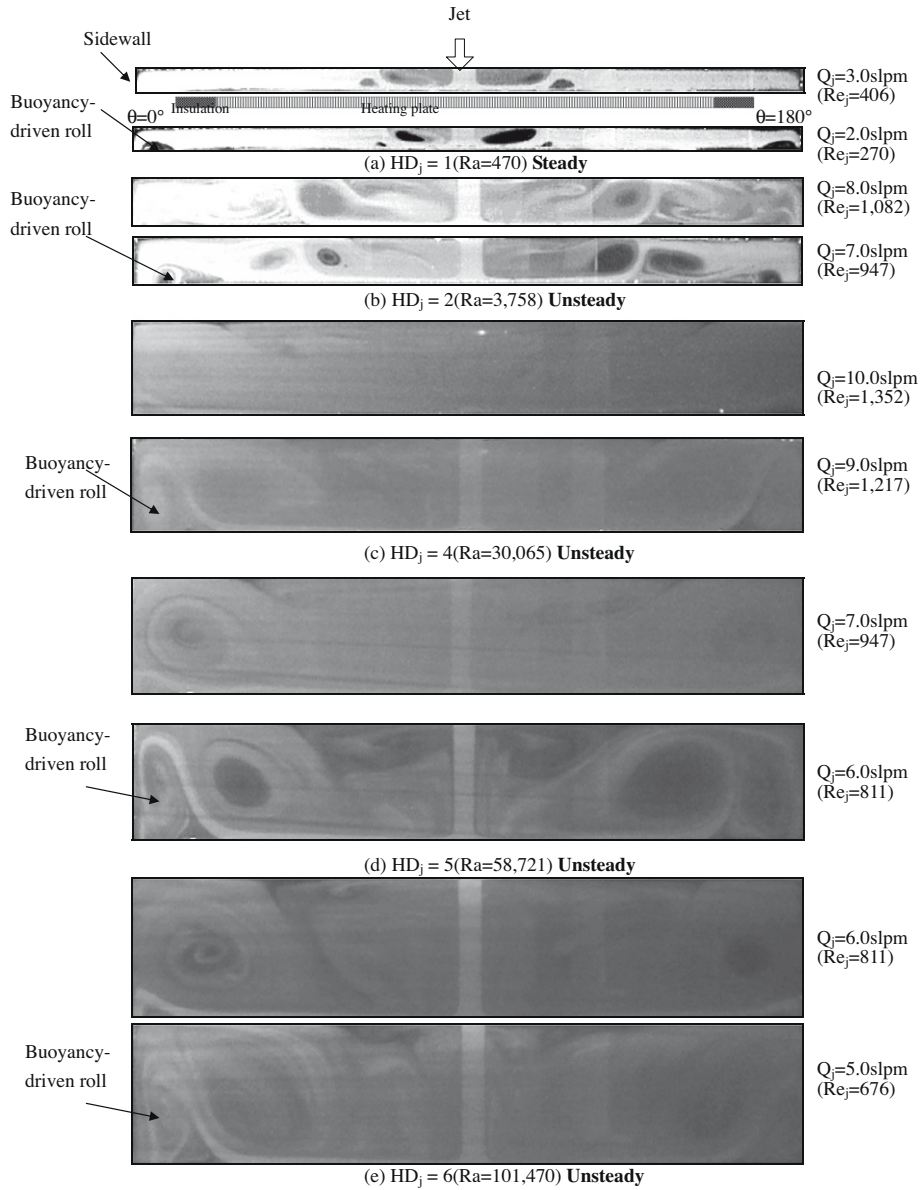
Fig. 4. Side view flow photos taken at the cross plane $\theta = 0°$ and $180°$ for various HD_j and Re_j at $\Delta T = 5$ °C.

HD_j raised from 4 to 6. For instance at $\Delta T = 5$ °C, the critical Q_j increases from 2.8 to 8.0 slpm for HD_j raised from 1 to 2 but decreases from 9.2 to 5.1 slpm for HD_j raised from 4 to 6 (Table 2). This variation of the critical Re_j for the onset of the buoyancy roll again can be attributed to the changes of the vortex flow structure for HD_j varied from 4 to 6 (Fig. 5). Furthermore, empirical equations are proposed to correlate the data given in Table 2 for the onset of the buoyancy-driven roll as

$$Gr/Re_{we}^2 = 34.0 \qquad (8)$$

for $1 \leqslant HD_j \leqslant 2$, $470 \leqslant Ra \leqslant 7516$, and $379 \leqslant Re_j \leqslant 1542$ and

$$(Gr/Re_{we}^5)^{0.25}/HD_j^{3.5} = 0.00125 \qquad (9)$$

for $4 \leqslant HD_j \leqslant 6$, $30,065 \leqslant Ra \leqslant 507,348$, and $811 \leqslant Re_j \leqslant 1542$.

When compared with our experimental data, the standard deviations of Eqs. (8) and (9) are, respectively, 2.2% and 5.7%.

3.3. Effects of HD_j on vortex flow characteristics

How the jet-disk separation distance affects the gas flow pattern at long time in the chamber with the disk unheated ($\Delta T = 0$ °C) is demonstrated in Fig. 6 by presenting the steady state side view flow photos for the cross plane $\theta = 0°$ and $180°$ for selected Q_j at various H. First, the results for the disk unheated manifest that at the lower Q_j of 1.0 slpm (Fig. 6(a)) the primary inertia-driven roll and the corner roll get bigger for an increase in HD_j as a result of stronger entrainment of the jet. Moreover, the primary and corner rolls contact with each other for $HD_j \geqq 4$ even at this low Q_j. In addition to the primary and corner rolls, the secondary roll is induced in the chamber for the higher Q_j of 3.0 slpm for $HD_j \leqq 4$ (Fig. 6(b)). According to the side view photos the primary roll is significantly bigger and the corner roll is only mildly bigger for HD_j increased from 1 to 4. But this is not the case for the secondary inertia-driven roll, as already discussed above. Note that as HD_j is raised from 4 to 5 the primary inertia-driven roll becomes relatively large for $Q_j = 3.0$ slpm, causing not only the

Table 2
Critical condition for the onset of the buoyancy-driven vortex roll for various H.

Separation distance (H, mm)	ΔT (°C)	Flowrate (Q_j, slpm)	Re_j	Ra	Gr/Re_{we}^2
10.0	5.0	2.8	379	470	34.9
	10.0	4	541	940	34.2
	15.0	5	676	1409	32.9
20.0	5.0	8	1082	3758	34.2
	10.0	11.4	1542	7516	33.7
	15.0–25.0	◎			
30.0	0.5–25.0	◎			
40.0	5.0	9.2	1244	30,065	207
	10.0	9.9	1339	60,130	358
	15.0	10.4	1407	90,195	486
	20.0	10.9	1474	120,260	590
	25.0	◎			
50.0	5.0	6.7	906	58,721	763
	10.0	7.2	974	117,442	1321
	15.0	8.0	1082	176,162	1605
	20.0	8.7	1177	234,883	1809
	25.0	9.1	1231	293,604	2067
60.0	5.0	5.1	690	101,470	2274
	10.0	6.0	811	202,939	3286
	15.0	7.0	947	304,409	3622
	20.0	7.5	1014	405,878	4207
	25.0	7.9	1068	507,348	4739

The buoyancy-driven vortex roll always appears in the range of Q_j tested in the present study, ◎.

secondary inertia-driven roll but also the corner roll to disappear. Thus, the entire chamber is occupied by the primary roll. Furthermore, at Q_j = 3.0 slpm the center of the primary roll begins to oscillate and the time-dependent vortex flow occurs as HD_j is raised from 5 to 6.

Next, the effects of the jet-disk separation distance on the steady vortex flow with the desk heated are exemplified in Fig. 5(a) by showing the steady state side view flow photos for ΔT = 5 °C and Q_j = 1.0 slpm at various H. The results clearly indicate that the buoyancy-driven roll which dominates in the outer region of the chamber is much bigger for a larger H. This large increase in the size of the buoyancy roll with the jet-disk separation distance is due to the large increase in the Rayleigh number associated with a small increase in H since Ra is proportional to H^3, as mentioned above. It is of interest to note that at the larger H (30.0–60.0 mm) the radial extent of the buoyancy roll

is so large and it directly contacts with the primary inertia-driven roll. However, the buoyancy force is much stronger than the inertia force as HD_j is raised from 3 to 6 in a such lower Q_j (=1.0 slpm), which in turn results in the growth of the buoyancy roll and the decay of the primary roll. For a higher Q_j of 3.0 slpm the results in Fig. 5(b) show that the secondary inertia-driven roll exists in the chamber for the small H of 10.0 and 20.0 mm. At the larger H ($\geq$30.0 mm) the primary and buoyancy rolls contact with each other for larger HD_j and the secondary roll does not appear. Besides, at this higher Q_j the growth of the primary roll with H is much stronger than buoyancy roll. In fact, we note a slight decay of the buoyancy roll for HD_j raised from 3 to 4, which is opposite to that for the lower Q_j of 1 slpm shown in Fig. 5(a). Furthermore, stronger mutual pushing of the primary and buoyancy rolls at a higher H causes the vortex flow to become time-dependent for HD_j raised to 5 and 6 in a such higher Q_j (=3.0 slpm).

3.4. Temperature distributions in vortex flow

In addition to the vortex flow characteristics presented above, selected results from the measured steady air temperature distributions in the vortex flow are shown in Fig. 7 along with the corresponding side view flow photos for Q_j = 1 slpm and ΔT = 5 °C for $H \geq$ 40.0 mm along a horizontal line at the middle horizontal plane between the disk and chamber top at θ = 0°. The non-dimensional air temperature Φ is defined as $(T - T_j)/(T_f - T_j)$. The air temperature increases slightly with the radial distance measured from the jet axis and reaches a maximum in the region when the wall-jet separates from the disk surface. For a further increase in the radial distance the air temperature starts to decline due to the presence of the buoyancy-driven roll and drops sharply near the sidewall of the chamber. A close examination of the data further reveals that at increasing jet-disk separation distance the temperature peak moves toward to the jet axis, reflecting the fact that we have a smaller primary inertia-driven roll and a larger buoyancy-driven roll for a higher HD_j. Thus the above nonmonotonic radial air temperature distributions result directly from the presence of the primary inertia-driven and buoyancy-driven vortex rolls in the chamber and the deflection of the impinging jet flow by these rolls. The above conclusion for the radial air temperature distributions is further substantiated by the results given in Fig. 8 for a slightly higher Q_j of 1.7 slpm.
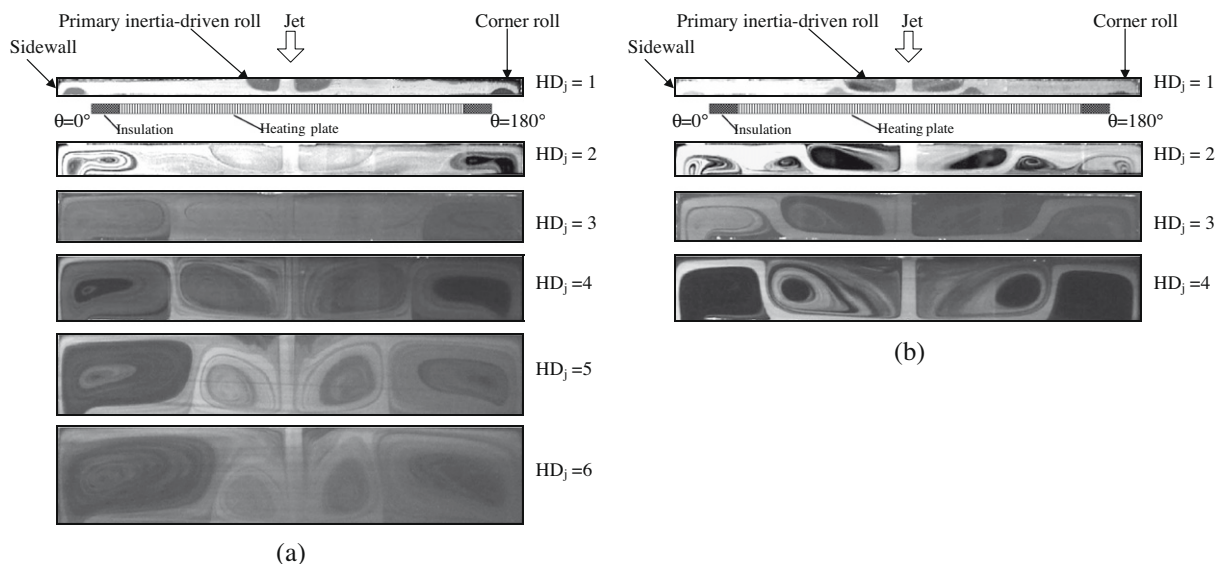

Fig. 5. Steady side view flow photos taken at the cross plane θ = 0° and 180° for various HD_j at ΔT = 5 °C for (a) Q_j = 1.0 slpm (Re_j = 135) and (b) Q_j = 3.0 slpm (Re_j = 406).

Fig. 6. Steady side view flow photos taken at the cross plane $\theta = 0°$ and $180°$ for various HD_j at $\Delta T = 0$ °C ($Ra = 0$) for (a) $Q_j = 1.0$ slpm ($Re_j = 135$) and (b) $Q_j = 3.0$ slpm ($Re_j = 406$).
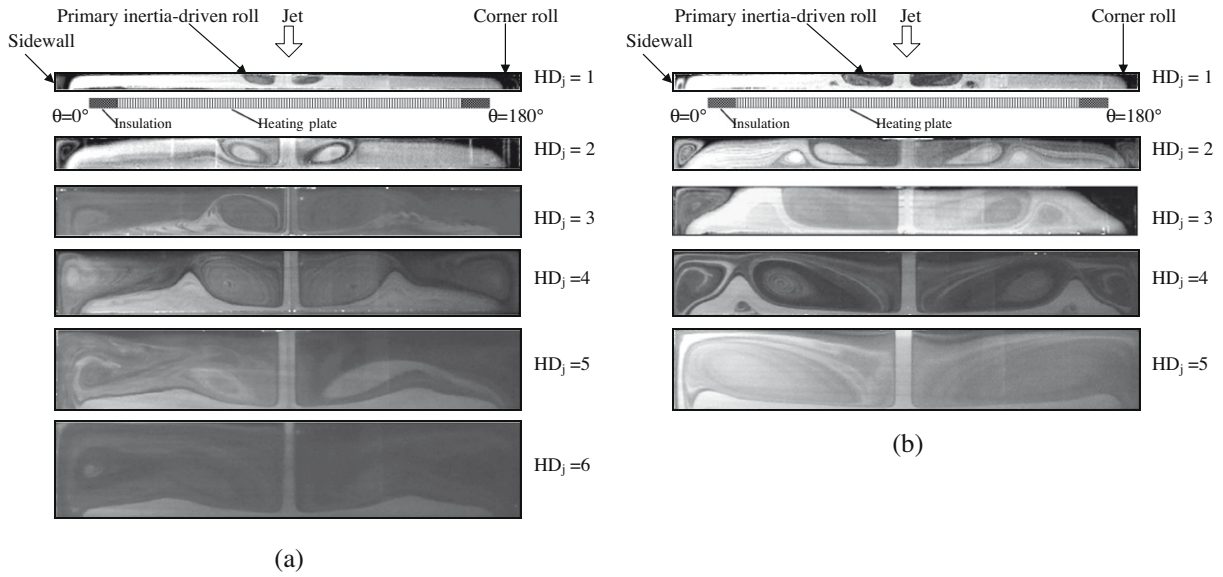

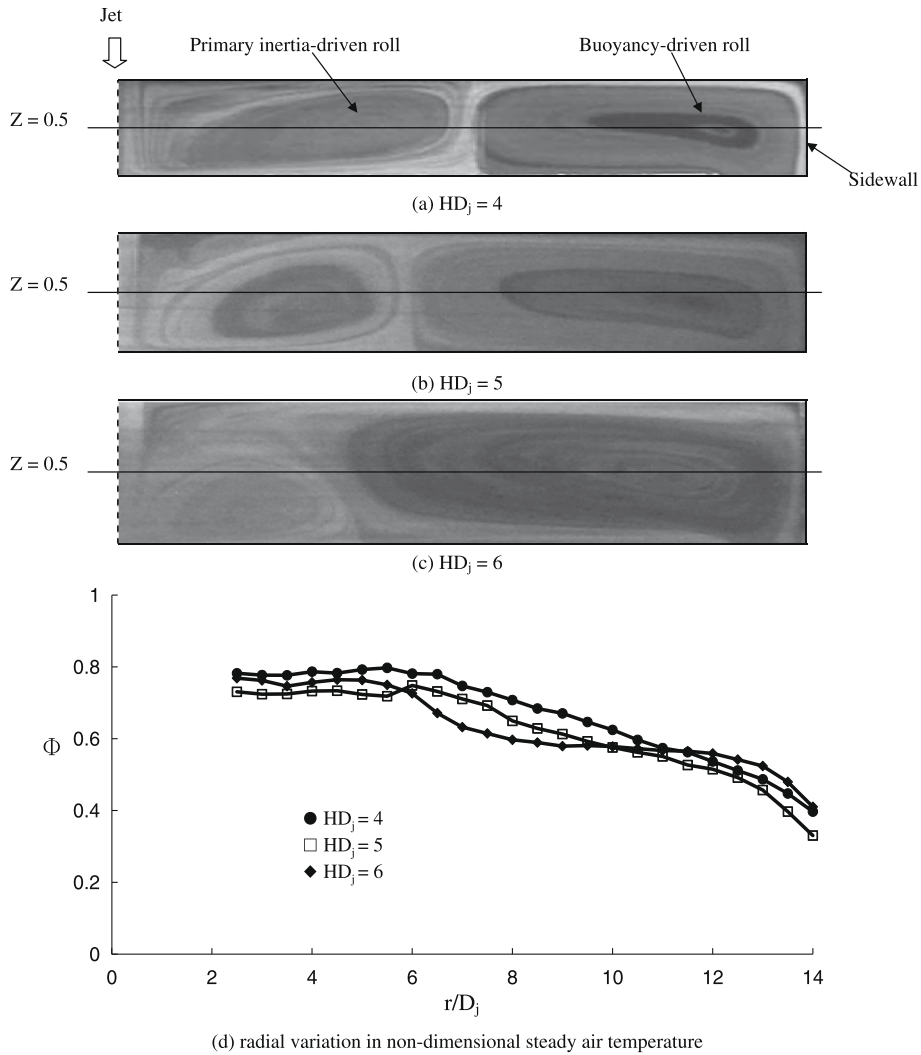**Fig. 7.** Radial variation in non-dimensional steady air temperature with $Re_j = 135$ ($Q_j = 1.0$ slpm) and $\Delta T = 5.0$ °C at $Z = 0.5$ on the vertical plane $\theta = 0°$ for $HD_j = 4$, 5, and 6.

Jet

Primary inertia-driven roll   Buoyancy-driven roll

Z = 0.5

Sidewall

(a) $HD_j = 4$

Z = 0.5

(b) $HD_j = 5$

Z = 0.5

(c) $HD_j = 6$

- $HD_j = 4$
- $HD_j = 5$
- $HD_j = 6$

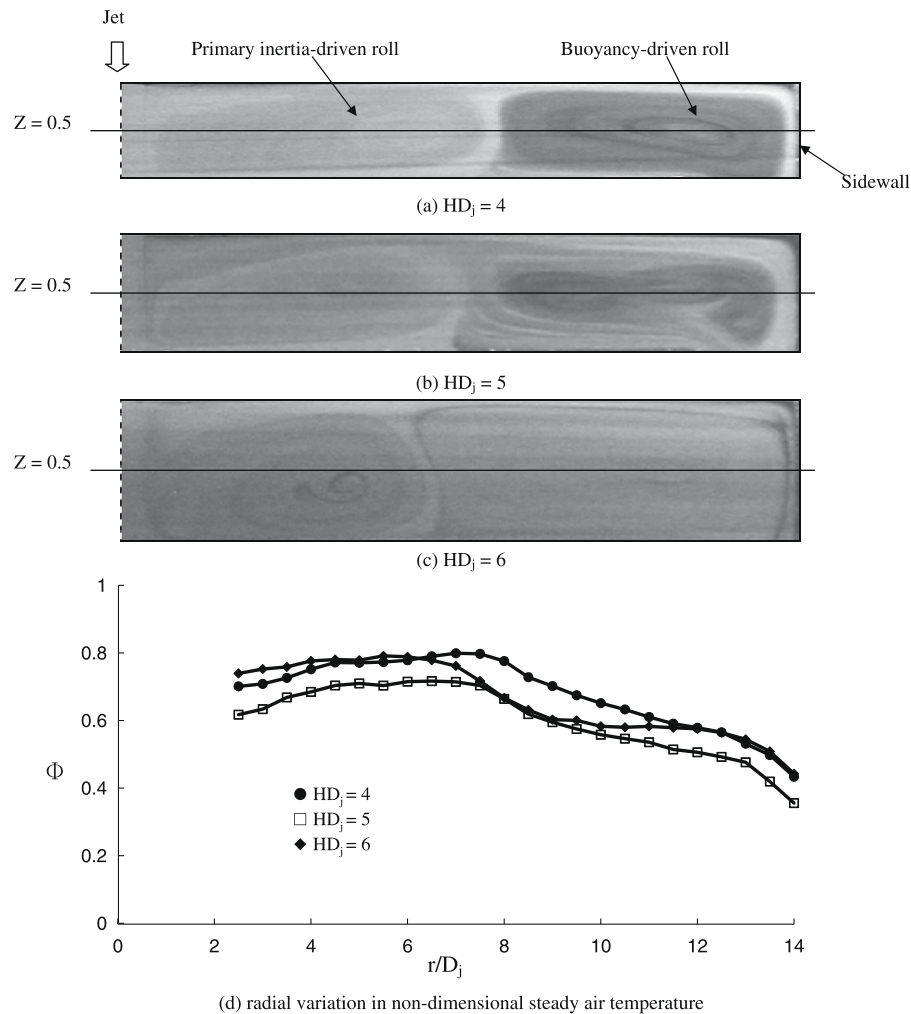(d) radial variation in non-dimensional steady air temperature

Fig. 8. Radial variation in non-dimensional steady air temperature with $Re_j = 230$ ($Q_j = 1.7$ slpm) and $\Delta T = 5.0$ °C at $Z = 0.5$ on the vertical plane $\theta = 0°$ for $HD_j = 4$, 5, and 6.

4. Concluding remarks

An experiment combining flow visualization and temperature measurement is conducted in the present study to explore how the jet-disk separation distance affects the steady mixed convective vortex flow resulting from a round air jet impinging onto a heated horizontal circular disk confined in a vertical cylindrical chamber. The major results obtained in the present study can be briefly summarized in the following:

1. The secondary inertia-driven roll does not appear at a larger jet-disk separation distance for $HD_j = 5$ and 6. Moreover, for HD_j raised from 1 to 3 the critical Re_j for the onset of the secondary roll becomes earlier but the opposite is the case when HD_j is raised from 3 to 4.
2. The critical Re_j for the onset of tertiary inertia-driven roll varies nonmonotonically with the jet-disk separation distance raised from 1 to 6 due to the complicate variations of the vortex flow structures with the jet-disk separation distance.
3. The buoyancy-driven roll always appears for $HD_j = 3$ even at a small temperature difference between the heated disk and injection air. Moreover, for HD_j increased from 1 to 2 the critical Re_j for the onset of the buoyancy-driven roll is delayed to a higher Re_j but the onset becomes earlier as HD_j is raised from 4 to 6.
4. For the cases with the disk unheated, the primary, secondary, and corner rolls all grow with HD_j except that the secondary roll decays as HD_j is raised from 3 to 4.

5. For the cases with the disk heated, at low Re_j both the primary inertia-driven roll and the buoyancy-driven roll get larger at increasing HD_j for a small jet-disk separation distance ($HD_j = 1$ and 2). But for $HD_j \geq 3$ the primary roll and buoyancy roll contact with each other, the primary roll decays and the buoyancy roll grows with the jet-disk separation distance at the lower Q_j of 1 slpm and the opposite is true at the higher Q_j of 3 slpm.
6. The nonmonotonic radial air temperature distributions are found to result from the presence of primary inertia-driven and buoyancy-driven vortex rolls in the chamber and the deflection of the impinging jet flow by these rolls.
7. Empirical equations are proposed to correlate the conditions leading to the onsets of the primary, secondary, tertiary, and buoyancy rolls.

References

[1] J.C. Hsieh, T.F. Lin, Effects of jet-to-disk separation distance on the characteristics of mixed convective vortex flow in an impinging air jet confined in a cylindrical chamber, Int. J. Heat Mass Transfer 48 (2005) 511–525.

[2] J.A. Fitzgerald, S.V. Garimella, A study of the flow field of a confined and submerged impinging jet, Int. J. Heat Mass Transfer 41 (1998) 1025–1034.

[3] G.K. Morris, S.V. Garimella, Orifice and impingement flow fields in confined jet impingement, J. Electron. Packaging 120 (1998) 68–72.

[4] G.K. Morris, S.V. Garimella, J.A. Fitizgerald, Flow-field prediction in submerged and confined jet impingement using the Reynolds stress model, J. Electron. Packaging 121 (1999) 255–262.

[5] J.C. Hsieh, T.C. Cheng, T.F. Lin, Characteristics of vortex flow in a low speed air jet impinging onto a heated disk in a vertical cylindrical chamber, Int. J. Heat Mass Transfer 46 (2003) 4639–4656.

[6] H.S. Law, J.H. Masliyah, Mass transfer due to a confined laminar impinging axisymmetric jet, Int. Eng. Chem. Fundam. 23 (1984) 446–454.

[7] D. Sahoo, M.A.R. Sharif, Numerical modeling of slot-jet impingement cooling of a constant heat flux surface confined by a parallel wall, Int. J. Thermal Sci. 43 (2004) 877–887.

[8] V.A. Chiriac, A. Ortega, A numerical study of the unsteady flow and heat transfer in a transitional confined slot jet impinging on an isothermal surface, Int. J. Heat Mass Transfer 45 (2002) 1237–1248.

[9] Z.H. Lin, Y.J. Chou, Y.H. Hung, Heat transfer behaviors of a confined slot jet impingement, Int. J. Heat Mass Transfer 40 (1997) 1095–1107.

[10] H.V. Santen, C.R. Kleijn, H.E.A. Van Den Akker, Mixed convection in radial flow between horizontal plates – I. Numerical simulations, Int. J. Heat Mass Transfer 43 (2000) 1523–1535.

[11] H.V. Santen, C.R. Kleijn, H.E.A. Van Den Akker, Mixed convection in radial flow between horizontal plates – II. Experiments, Int. J. Heat Mass Transfer 43 (2000) 1537–1546.

[12] H.J. Poh, K. Kumar, A.S. Mujumdar, Heat transfer from a pulsed laminar impinging jet, Int. Commun. Heat Mass Transfer 32 (2005) 1317–1324.

[13] H.S. Law, J.H. Masliyah, Numerical prediction of the flow field due to a confined laminar two-dimensional submerged jet, Comput. Fluids 12 (1984) 199–215.

[14] K. Jambunathan, E. Lai, M.A. Moss, B.L. Button, A review of heat transfer data for single circular jet impingement, Int. J. Heat Fluid Flow 13 (1992) 106–115.

[15] R. Viskanta, Heat transfer to impinging isothermal gas and flame jets, Exp. Thermal Fluid Sci. 6 (1993) 111–134.

[16] G. Wahl, Hydrodynamic description of CVD processes, Thin Solid Films 40 (1977) 13–26.

[17] D.I. Fotiadis, S. Kieda, Transport phenomena in vertical reactor for metalorganic vapor phase epitaxy, J. Crystal Growth 102 (1990) 441–470.

[18] A.H. Dilawari, J. Szekely, A mathematical representation of a modified stagnation flow reactor for MOCVD application, J. Crystal Growth 108 (1991) 491–498.

[19] C.Y. Soong, Gasdynamic characteristics and thermal-flow design of metal organic chemical vapor deposition reactors for semiconductor thin-films, Instrum. Today 25 (3) (1993) 71–82.

[20] S.P. Vanka, G. Luo, N.G. Glumac, Parametric effects on thin film growth and uniformity in an atmospheric pressure impinging jet CVD reactor, J. Crystal Growth 267 (2004) 22–34.

[21] G. Luo, S.P. Vanka, N. Glumac, Fluid flow and transport processes in a large area atmospheric pressure stagnation flow CVD reactor for deposition of thin films, Int. J. Heat Mass Transfer 47 (2004) 4979–4994.

[22] W. Burwash, W. Finlay, E. Matida, Deposition of particles by a confined impinging jet onto a flat surface ar $Re = 10^4$, Aerosol Sci. Technol. 40 (2006) 147–156.

[23] S.J. Kline, F.A. McClintock, Describing uncertainties in single-sample experiment, Mech. Eng. 75 (1953) 3–8.